Time-resolved momentum imaging system for molecular dynamics studies using a tabletop ultrafast extreme-ultraviolet light source

Etienne Gagnon,[1] Arvinder S. Sandhu,[1,2] Ariel Paul,[1] Kim Hagen,[1] Achim Czasch,[3] Till Jahnke,[3] Predrag Ranitovic,[4] C. Lewis Cocke,[4] Barry Walker,[5] Margaret M. Murnane,[1] and Henry C. Kapteyn[1]
[1]*JILA, University of Colorado at Boulder, Boulder, Colorado 80309-0440, USA*
[2]*Department of Physics, University of Arizona, Tucson, Arizona 85721-0081, USA*
[3]*Institut für Kernphysik, Johann Wolfgang Goethe Universität, Frankfurt 60438, Germany*
[4]*J. R. MacDonald Laboratory, Physics Department, Kansas State University, Manhattan, Kansas 66506, USA*
[5]*Department of Physics, University of Delaware, Newark, Delaware 19716, USA*

(Received 28 March 2008; accepted 28 April 2008; published online 5 June 2008)

We describe a momentum imaging setup for direct time-resolved studies of ionization-induced molecular dynamics. This system uses a tabletop ultrafast extreme-ultraviolet (EUV) light source based on high harmonic upconversion of a femtosecond laser. The high photon energy (around 42 eV) allows access to inner-valence states of a variety of small molecules via single photon excitation, while the sub--10-fs pulse duration makes it possible to follow the resulting dynamics in real time. To obtain a complete picture of molecular dynamics following EUV induced photofragmentation, we apply the versatile cold target recoil ion momentum spectroscopy reaction microscope technique, which makes use of coincident three-dimensional momentum imaging of fragments resulting from photoexcitation. This system is capable of pump-probe spectroscopy by using a combination of EUV and IR laser pulses with either beam as a pump or probe pulse. We report several experiments performed using this system. © *2008 American Institute of Physics.*
[DOI: 10.1063/1.2930869]

I. INTRODUCTION

Coherent beams of extreme-ultraviolet (EUV) light can be generated using the extreme nonlinear-optical process of high harmonic generation (HHG).[1] This process frequency upconverts an intense ($>10^{14}$ W cm^{-2}), ultrashort (<25 fs), laser pulse from the visible-near IR into the EUV region of the spectrum, at photon energies of $10->1000$ eV.[2,3] Because the pulse duration of the generated high harmonic light is shorter than that of the driving laser pulses—easily in the range of <1 fs duration[4]—the resulting EUV pulses represent a unique and powerful probe of ultrafast electronic, atomic, and molecular dynamics.[5,6] Recent advances in technology, such as use of few cycle pulses for EUV generation[7,8] and carrier-envelope-phase stabilization[9–11] have opened up a number of possibilities in the field of attosecond dynamics and attosecond control with high harmonic sources.

The ability to make very short pulses of ionizing radiation opens the intriguing possibility of studying the dynamics of ionized and highly excited molecular systems. This topic is of interest for understanding radiation chemistry at the most-fundamental level. Nevertheless, experiments in this area have been slow to reach fruition, because the photon flux achievable by using ultrafast short-wavelength light sources is insufficient to implement a typical pump-probe experiment. Generally, in a pump-probe study, a significant fraction of a target sample must be excited by using a pump pulse, while the probe pulse then directly follows dynamic changes in optical absorption or other characteristics.

As an alternative to directly exciting a molecule by using a single x-ray photon, a number of experiments[12–18] have observed dynamics in molecules excited or ionized using multiphoton absorption of infrared, visible, or ultraviolet laser pulses. However, while these studies are quite interesting and contribute to our understanding of molecular dynamics, the insights gained primarily address molecular behavior in the artificial environment of a focused intense laser field. In particular, in the case of ionization-induced dynamics, multiphoton ionization (MPI) nearly inevitably strips electrons sequentially from an atom or molecule. The reason for this is simple—strong-field ionization has few selection rules, and simply rips off electrons starting with the most-loosely bound ones. Any excited transition-state ions that might be created during the process are rapidly ionized themselves. MPI-induced dynamics thus fundamentally differ from the typical ionizing radiation interaction that occurs in nature. In the case of molecular photoionization, inner-shell or inner-valence ionization results in the population of many highly excited ionized states that determine the subsequent dynamics. These dynamics are directly relevant to naturally occurring processes such as solar radiation-induced processes in planetary atmospheres.[19,20]

Thus, there exists considerable motivation to develop new experimental methodologies that use ultrashort pulses of high-energy radiation to access the inner electrons and highly excited states of molecules that are not directly accessible using multiphoton techniques.[21] The first issue that must be resolved is to obtain pulses of ionizing radiation with duration in the femtosecond range—preferably $\ll 100$ fs—since

these highly excited systems will have exceptionally rapid dynamics. In the past, different schemes have been used to generate EUV light for spectroscopic purposes, e.g., synchrotrons, plasma discharges, etc. These sources have limited time resolution, and are thus incapable of observing these processes in real time. Since real-time observation can also facilitates the potential for real-time control, there is a strong incentive to develop ultrashort-pulse EUV sources. Recently developed vuv and x-ray free electron lasers; i.e., "fourth generation" light sources, generate intense pulses of ionizing radiation with femtosecond time duration.[22,23] However, laser-based sources will continue to have a major advantage over these sources in terms of temporal resolution,[4,7] timing synchronization in pump-probe experiments, in pulse repetition rate, and in terms of accessibility as a small-scale laboratory source. EUV pulses generated using high harmonic generation can have pulse duration as short as ~130 as[7] which is more than sufficient to capture ultrafast molecular dynamics, and even directly observe purely electronic dynamics.

In this paper, we demonstrate that it is possible to effectively make use of these laser-based EUV sources for direct studies of molecular dynamics induced by ionizing radiation. To accomplish this, we combined two state-of-the-art technologies. First, we need to optimize the conversion efficiency of the HHG light source, to deliver as much of the generated light as possible onto a target. Second, we need to employ detection techniques that are highly selective to allow us to detect the products of x-ray dissociation—even when most of the target sample is not affected by the incident radiation. In this article, we discuss improvements in the driving laser repetition rates, high harmonic efficiency, and beam delivery optics, and the implementation of efficient spectroscopic and imaging scheme for the experiment. Three-dimensional momentum spectrometry techniques with 4π collection efficiency and coincident electron/ion detection are, in our view, some of the most promising methods of exploring atomic and molecular dynamics with these laser-based sources. We discuss the implementation of one such technique, namely, the cold target recoil ion momentum spectroscopy[24–26] (COLTRIMS) reaction microscope, in conjunction with our laser-based femtosecond EUV source. By using this novel approach, we have demonstrated the use of a femtosecond EUV source to initiate the photofragmentation dynamics of highly excited states in small molecules.[21] The dynamics are then probed by a femtosecond IR pulse. In this article, we discuss the techniques and methods which we believe represent a critically important methodology for the study of pump-probe EUV molecular spectroscopy in the femtosecond and attosecond regime.

II. EXPERIMENTAL APPARATUS

The experimental setup consists of two major components: the laser system and high harmonic upconversion setup, and the momentum imaging spectrometer. The laser system will be discussed first, followed by a summary of the setup used for high harmonic generation (HHG). More in-depth descriptions of the HHG process have appeared in past work.[27–31] In our current discussion, we emphasize the experimental implementation of a reliable tabletop EUV "beamline," and the particular technical difficulties involved in efficient EUV generation and delivery for this experiment.

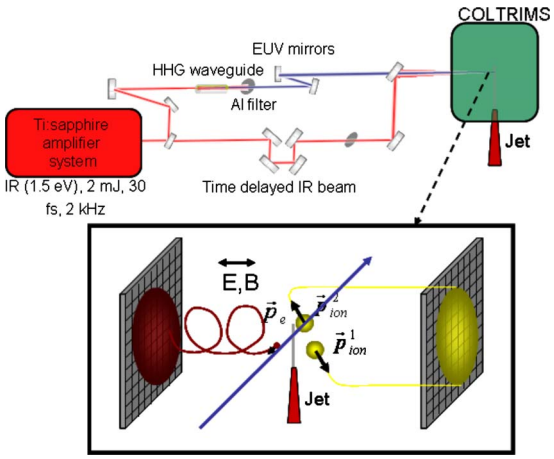

FIG. 1. (Color online) (Top) Schematic of the experimental setup showing the Ti:sapphire amplifier system, the pump/probe geometry, and the detector. The EUV beam is produced through HHG in a waveguide. The EUV is then filtered and focused to the interaction region by using multilayer EUV mirrors. The IR is time delayed using an adjustable beam path length. (Bottom) Schematic of the charged particle detection geometry of the COLTRIMS detector that allows for momenta reconstruction.

A schematic of the experimental setup is shown in Fig. 1 (top). The Ti:sapphire amplifier system supplies an ~2 mJ IR beam, which is split, by using a beam splitter. Part of the beam (~1.2 mJ) is used to generate EUV light through HHG. The remainder of the beam (~0.8 mJ) is time delayed and recombined with the EUV-pump beam. The EUV and IR beams are then spatially overlapped on a molecular gas jet, which acts as our interaction region within the COLTRIMS detector.

Figure 1 (bottom) shows a schematic of the charged particle detection setup inside the COLTRIMS: charged particles are generated by interacting with photons (either IR or EUV) and are guided to either side of the position-sensitive detectors by electric and magnetic fields.

The details of the individual components of Fig. 1 will be discussed in greater details in the following text.

A. Laser system

The laser system used in these experiments is a titanium-doped sapphire-based ultrafast laser oscillator-amplifier system patterned after the KMLabs Inc. Dragon™ system. This laser uses a 10 fs kerr-lens mode locked ti:sapphire laser oscillator[32,33] followed by a single stage, ten-pass, Ti:sapphire-based laser amplifier[34,35] with a ring geometry using a cryogenically cooled laser amplifier crystal to avoid thermal lens distortions. The laser generates pulses of 2 mJ energy, with sub--30-fs pulse duration, at a pulse repetition rate variable between 1 and 3 kHz. Most experiments were performed at 2 kHz. The laser system employs a standard grating-based stretcher and compressor, which makes possible excellent amplifier spatial mode quality at high power. The output beam has a well-behaved focus with an M^2 of 1.1—1.4.

B. High harmonic upconversion into the EUV

The conversion efficiency of the HHG process is determined by two factors: (1) the microscopic generation process (three-step model)[36,37] and (2) macroscopic propagation effects; i.e., the phase matching between the fundamental IR driving laser field and the EUV field. Without phase matching,[38,39] the EUV field will build up over a short distance (called the coherence length, L_c) before destructive interference limits the signal intensity because the phase of the generated harmonics slips by π compared to the driving laser. In this work, we use a 2.5 cm long, 150 μm diameter gas-filled waveguide to balance the dispersion of the neutral gas, plasma, and waveguide, so that the residual wave vector mismatch (Δk) is zero. The wave vector mismatch can be expressed as

$$\Delta k = q k_\omega - k_{q\omega} \approx q\left\{P\left(\frac{2\pi}{\lambda}\Delta\delta - \eta\left[\frac{2\pi}{\lambda}\Delta\delta + N_{\mathrm{atm}} r_e \lambda\right]\right) - \frac{u_{11}^2 \lambda}{4\pi a^2}\right\},$$

where q is the order of the harmonics, ω is the fundamental laser frequency, λ is the fundamental wavelength, η is the ionization fraction, P is the gas pressure, N_{atm} is the number density at 1 atm, r_e is the classical electron radius, and $\Delta\delta = \delta(\lambda) - \delta(\lambda/q)$ is the difference in the index of refraction at the fundamental and harmonic frequencies for the gas at 1 atm.[38,40] The last term in Eq. (1) is the contribution from the waveguide, where u_{11} is the first zero of the Bessel function J_0 and a is the radius of the waveguide. In Eq. (1), the first term within the parentheses corresponds to the neutral gas contribution, the term within square brackets corresponds to the plasma contribution, and the last term within the curly brackets takes the waveguide contribution to the phase mismatch into account. When Δk is nearly 0, the phase velocity of the EUV light matches the phase velocity of the IR beam inside the waveguide. Thus, the EUV signal can build up coherently along the propagation direction.

The laser intensity at the entrance of the waveguide is typically $(1-5)\times 10^{14}$ W/cm^2. The Ar gas pressure inside the EUV waveguide is adjusted for optimal phase matching, typically in the range of 10–80 torr, depending on the laser pulse intensity and duration, and which harmonics are to be optimized. The waveguides are made of fused silica and are separated into three sections [as can be seen in Fig. 2(a)]: a 2.5 cm long constant pressure section between the gas inlets and two 5 mm long, differential pumping sections between the gas inlets and the ends of the waveguide.

The quality of the output spatial mode of the HHG waveguide is important. Because the molecular dynamics experiments were performed in an EUV-pump/IR-probe geometry (see Sec. III), it is vital that the focused beams (both IR and EUV) be well behaved (i.e., a single intense smooth region without any hot spots) in the interaction region of the detector. For the EUV beam, this can only be achieved if the HHG output spatial mode is well behaved.

The quality of the EUV mode depends both on the propagation of the generating IR pulse through the waveguide and the degree of phase matching. Marcatili and Schmeltzer[41] performed a detailed analysis of beam propagation inside a hollow core waveguide and found that even for bend radii on the order of many meters, the propagation loss can be significant and higher order modes can be launched. To minimize bending, the HHG waveguides are supported by a V-groove mount.[42] The design of the waveguide holder is shown in Fig. 2(c). The modular design makes it possible to insert various length V-groove center sections. The end sections are precisely machined to allow a good vacuum seal at the ends of the waveguide, without applying any stress that could introduce bending.

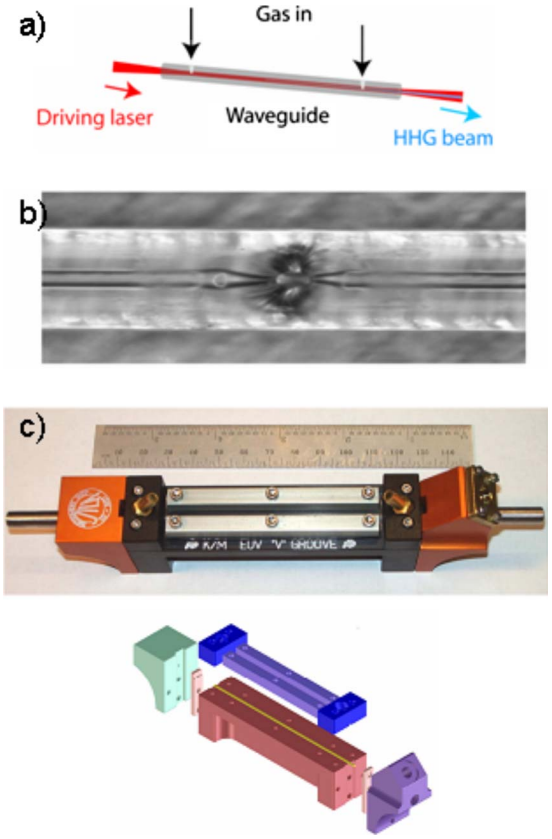

FIG. 2. (Color online) (a) Schematic of the three section EUV waveguide. Two gas inlets allow a constant pressure to be maintained in the center region while the end sections are differentially pumped. (b) Microscope image of laser-created hole in EUV waveguide. The inner capillary is left minimally deformed by the hole. The hourglass shape seen in the picture is due to the lensing effect of the melted outer wall of the capillary. (c) Picture of a HHG waveguide V-groove holder engineered to ensure good mode propagation and low loss. The middle section can be changed to allow different length waveguides to be used.

Another important engineering aspect of the waveguides is the manufacture of the gas insertion holes. To prevent disruption of the propagating IR laser mode due to uneven surfaces or obstacles that might be produced by abrasive cutting/drilling methods, a CO_2 laser is used to drill holes into the capillary for the gas inlets. Control of the CO_2 laser intensity and focusing parameters allows the formation of smooth holes. The result of such a laser-created hole can be seen in Fig. 2(b).

When using an ~20 fs driving pulse, the HHG signal intensity shows a broad pressure-tuned phase matching structure, peaked around 30–40 torr. Because the optimal phase matching conditions span a few (i.e., ~2) cycles of the driv-

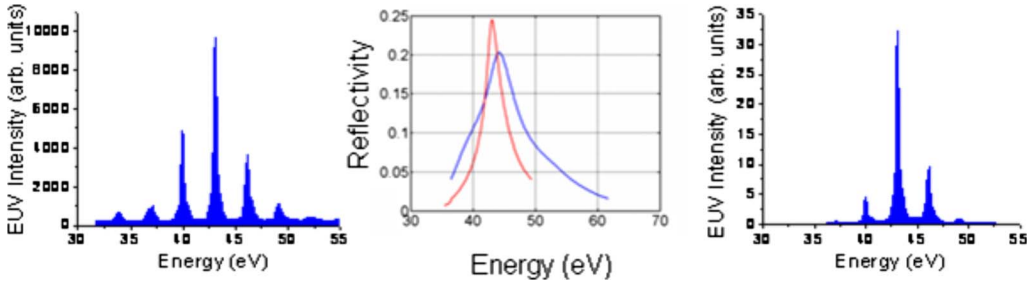

FIG. 3. (Color online) (Left) Sample EUV spectrum obtained with a 30 fs driving laser pulse. The emission consists of a comb of harmonics centered at ~43 eV. (Middle) Reflectivity of Mo/Si multilayered mirror as a function of photon energy for a single reflection. The blue curve is a broadband reflection. The red curve is narrow-band reflection. (Right) Sample spectrum of the EUV beam after two reflections from the multilayer narrow-band EUV mirrors used in the experiments described herein.

ing laser pulse, the HHG output in the time domain will consist of a short train of pulses. For many molecular dynamics experiments, where processes occur on a time scale of a few femtoseconds or longer, this temporal resolution is adequate. (To generate subfemtosecond duration EUV pulses, very short driving laser pulses can be used.[4]) In the spectral domain, EUV beam generated from phase-matched HHG with a >20 fs driving laser pulse generally spans a number of (i.e., ~3–5) harmonic orders [see Fig. 3(a)].

Most molecular dynamics studies can benefit from the narrowest possible spectral bandwidth consistent with the desired time duration. Such bandwidth selection can be done in a number of ways, including using gratings or specially designed multilayer mirrors. However, wavelength selection using a grating will result in broadening the pulse envelope in the time domain, with a corresponding reduction in temporal resolution. This time dispersion can be compensated for using a dual-grating compensated EUV monochromator.[43] However, this greatly increases the complexity of the system. Multilayer mirrors, on the other hand, can select a narrow region of the spectrum by using a simple optical setup and with minimal temporal dispersion. The disadvantage is that the typical spectral bandwidth of ~4–5 eV at 43 eV that can be obtained by using a multilayer does allow some of the neighboring harmonic orders to reflect, limiting the spectral purity of the light.

In our setup, we use two multilayer mirrors to energy select and refocus the high harmonics [see Fig. 3(b)]. We use a small-angle, z-fold configuration, consisting of a flat mirror and 1 m radius of curvature mirror, both of which are Mo/Si coated for 30 nm wavelengths. The reflection spectrum of these mirrors can be tuned from narrow band to broadband, depending on choice of coating parameters. In our case, ten periods of Mo/Si were used, each with a thickness of ~15.5 nm, with a molybdenum/silicon thickness ratio of ~1/4. Figure 3(c) shows the resulting spectrum after two bounces from these multilayer mirrors. The peak reflectivity is ~6%, while the finite bandwidth means that, in addition to the central reflected harmonic, two sideband harmonics will also be reflected with less efficiency ($\leq$1%). These sideband harmonics will contribute slightly to the data, and must to be taken into account in the analysis.

The multilayer pair used in these experiments has a throughput of ~6%. This gives sufficient flux for many applications, as we demonstrate. However, further improvements in the mirror reflectivity can rapidly increase the throughput, and thus the flux on target. Mo/Si is the most commonly used multilayer pair, since it allows for high reflectivity at 13 nm. However, these are not the optimum materials for high reflectivity at 30 nm. Increasing the reflectivity from ~20%–25% per mirror to ~40%–45% per mirror is feasible using a Mg/SiC layer pair, and will increase the beamline throughput ×(3–4). We also note that some experiments can use broad-band-width illumination, in which case a high-efficiency grazing incidence toroidal reflector would refocus the EUV beam into the target region with considerably less loss.

C. Pump-probe beam path

For the molecular dynamics experiments, we used two different beam path geometries in an EUV-pump/IR-probe configuration, as shown in Fig. 4. The beam path geometry shown in Fig. 4(a) was used for the experiment described in Sec. IV. The beam path geometry shown in Fig. 4(b) was later implemented for subcycle resolution experiments, where interferometric mechanical stability is required.

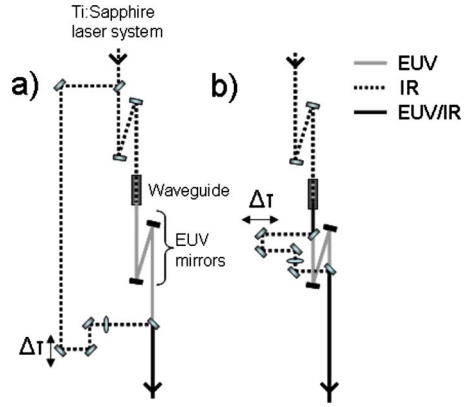

FIG. 4. (Color online) Schematic of pump-probe beam paths implemented in our experiments. The dashed line corresponds to the IR beam. The gray line is the EUV beam, while the black line corresponds to both the IR and the EUV beams together. In both geometries, part (a) or all (b) of the IR pulse is focused into a 150 μm diameter waveguide to generate EUV through HHG. Multilayer EUV mirrors are used to filter and focus the EUV beam to the interaction region. The IR pulse beam path is adjustable in length to vary the time delay between the EUV and IR pulses. The first geometry (a) has maximum flexibility whereas (b) allows interferometrically stable measurements.

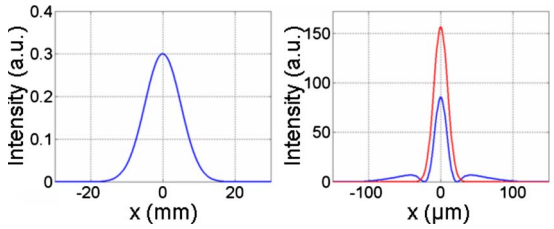

FIG. 5. (Color online) Computed profile of IR beam focused into the sample chamber, after reflection from the beam recombining mirror with a 3 mm hole in the center. (Left) IR beam as a $1/e2$ radius of 10 mm before the 75 cm lens. (Right: red) Focal spot inside the detector using a regular mirror (without a hole in the center). (Right: blue) Focal spot when mirror with a hole is used in the beam bath.

In the setup of Fig. 4(a), the pump and probe beamlines are split before the EUV waveguide. A beamsplitter directs ~70% of the light from the laser into the HHG upconversion waveguide. The EUV output mode is imaged onto the center of the detector using a multilayer mirror with a 1 m radius of curvature. The IR beam passes through a variable time delay and is then recombined with the EUV beam by using a mirror with a 3 mm hole drilled in the center.

The variable optical delay for pump-probe experiments is adjusted by using a motorized stage with 50 nm step size, corresponding to a time step of 0.33 fs (since the delay is double passed) and with a total travel of 5 cm (Melles Griot Linear Motorized Stage). However, the smallest repeatable step size was found to be 100 nm. After the optical delay, the IR beam is focused into the detector chamber using a 75 cm or 1 m focal length lens placed before the pump-probe recombining mirror. Because of the hole in this mirror, which effectively acts as a reverse aperture, the mode of the IR beam is modified upon reflection. Figure 5 shows a calculation that estimates this effect. In this calculation, the focal spot size and shape of the initial IR beam incident on the recombining mirror has a Gaussian profile with $1/e^2$ radius of 10 mm. The result shows that while the IR beam focused energy is reduced by the hole, the focused $1/e^2$ spot size is only a few microns smaller than without the hole. The introduction of side lobes contributes only slightly to the background counts. The spot size is approximately 50 μm diameter and the peak intensity is reduced by ~40% from its original value.

The EUV spot diameter in the setup is also estimated to be on the order of 50 μm. This estimate assumes proper one-to-one imaging of waveguide output using the 1 m radius of curvature multilayer mirror, and that the EUV output mode from the waveguide follows the 12th power of the first order Bessel function corresponding to the lowest-order mode of the driving laser pulse in the waveguide. This beam spot size is consistent with the observed divergence of the beam, of ~1 mrad. The 12th power corresponds to the effective nonlinear order of the HHG process, which corresponds approximately to the number of photons required to ionized the nonlinear medium, rather than the harmonic order (q) being generated.[44,45]

Obtaining good spatial and temporal overlap between the IR and EUV beams is achieved by matching the IR beam with the residual IR light copropagating with the high order harmonics, after the two beams exit the detector chamber. A cross correlation in a frequency-doubling crystal is used to find the temporal overlap. To achieve spatial overlap, a lens placed past the detector chamber intersects the EUV and IR paths, and a pinhole is placed at the point that images the interaction region in the chamber. The beams are then adjusted for maximum transmission through the pinhole. The EUV beam is assumed to have an output mode similar to the copropagating IR (scaled by the 12th power). Because of this assumption, it is paramount that the EUV waveguide be properly mounted and aligned to obtain a good fundamental mode, as was discussed in Sec. II.

The beam path geometry described above allows maximum flexibility for beam steering and adjustment of the intensity and polarization of the IR beam. The setup exhibits excellent long term stability, allowing data acquisition for periods of days without any need for realignment even with no active feedback on the beam pointing. However, because the EUV and IR beams propagate along separate paths for ~4 m, this setup lacks the interferometric stability required for 800 nm subcycle resolution experiments.

The second beam path geometry shown in Fig. 4(b) addresses this stability issue, at some cost in flexibility. In this geometry, the beam is split after the EUV waveguide using by a mirror with a hole, allowing the EUV beam to pass through while reflecting an annulus of the copropagating IR. This design is possible because of the difference in divergence between the EUV and IR beams exiting the waveguide. The EUV beam follows the same path as in the previous geometry and the waveguide output is imaged in the interaction region. The IR propagates through a variable length path and is also imaged to the center of the interaction region using a 50 cm focal length lens. It is then recombined with the EUV beam by using another mirror with a hole in the center.

In these interferometric experiments, to implement smaller delay steps ($\ll\lambda$) than are possible using the motorized translation stage, we use a closed-loop, piezoactuated, translator stacked on top of the motorized long travel stage. Overlapping the two beams temporally and spatially is achieved in the same fashion as in the previous beam geometry. Changes in the time delay will also introduce changes in the imaging condition of the IR. To minimize this effect, this beam path geometry can only be used for small time delays (on the order of 100 fs).

Because of the reduced path difference between the two beams (EUV and time delayed IR), this second beam geometry exhibits interferometric stability in a controlled laboratory environment. However, the compact geometry makes independent adjustment of the IR beam's intensity and polarization more difficult.

The EUV beam delivers $\sim 10^6$ photons/pulse into the interaction chamber in a 50 μm diameter spot. The IR intensity could be varied from 5×10^{12} to 5×10^{13} W/cm^2. In both geometries, the EUV mirrors were mounted in vacuum on remotely controlled motorized mirror mounts to steer the beam.

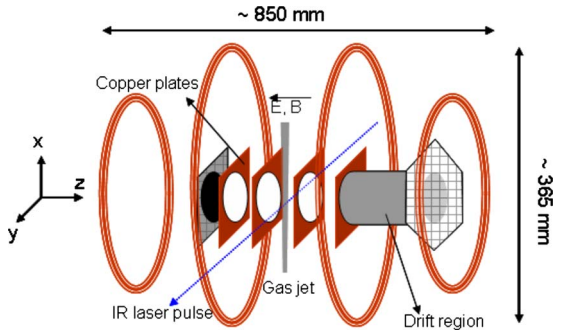

FIG. 6. (Color online) Schematic detection region geometry of the reaction microscope. The charged particles are guided to each side of the detector by a constant electric field generated by a series of copper electrodes, and by a magnetic field generated by copper coils. The interaction region consists of a supersonic molecular gas jet directed upward, perpendicular to the direction of the EUV and IR beams.

D. The interaction chamber

A simplified schematic of the reaction microscope is shown in Fig. 6. A pair of time- and position-sensitive detectors, combined with electric and magnetic fields allow for 4π collection efficiency of both electrons and ions, onto separate detectors. The detectors and supporting electronics were supplied by RoentDek Handels GmbH. The time and position information makes it possible to fully reconstruct the momenta of the particles detected. This calculation requires knowledge of the initial and final positions of the charged particle. It also requires constant and well-characterized electric and magnetic fields. The individual components of the spectrometer (copper electrodes, drift region, meshes, and copper coils), of the detector (delay line and microchannel plates), and of the molecular gas jet (interaction region) are described in detail below.

E. Gas target

A supersonic molecular gas jet supplies cooled molecules to the interaction region. A cross section of the interaction region, the gas jet assembly, and the jet catcher are shown in Fig. 7.

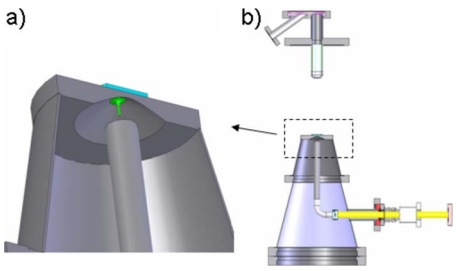

FIG. 7. (Color online) (a) Close-up of the nozzle and skimmer assembly used to generate the supersonic molecular gas jet. The conical shape of the chamber and of the area around the skimmer helps increase the pumping efficiency and keeps the pressure low in that region. (b) Gas jet and catcher assembly. The gas jet chamber and the catcher were engineered to be as close to the interaction region as possible. This helps keeping the pressure low in the main chamber during gas jet operation. The position of the tube bringing in the gas can be adjusted. Side to side adjustment ensures that the nozzle is centered on the skimmer. Up and down adjustment controls the gas density and the dispersion of the gas jet after the skimmer.

The gas jet originates in a supersonic expansion of the molecular gas through a 30 μm diameter nozzle. The nozzle backing pressure is $\sim$1 atm, while the exit region is kept at $\sim 5\times 10^{-5}$ torr by using a 2000 l/s turbomolecular pump (Leybold Mag 2000). A low divergence section of the supersonic expansion is selected by using a 300 μm skimmer, approximately 13 mm downstream from the nozzle. The skimmer also serves as barrier for differential pressure between the gas jet chamber and the detector chamber. As can be seen in Fig. 7, the gas jet chamber is conical. This geometrical shape enhances the gas conductance and helps to efficiently evacuate the background gas to maintain the gas jet chamber at a low pressure. This in turn helps the supersonic molecular beam formation. The skimmer is also cone shaped to reduce possible backscattering that would be detrimental to the supersonic flow.

After the skimmer, the molecular beam still has some divergence. The amount of divergence can be adjusted by varying the distance between the nozzle and the skimmer. For a distance of 13 mm between the nozzle and the skimmer, the gas target in the interaction region situated $\sim$9 cm above the skimmer has a diameter of 4 mm. This translates into an extended region of interaction along the beam propagation axis. The other two transverse dimensions are confined by the focused laser beam diameter. The longitudinal dimension will introduce a slight uncertainty in the initial position of the molecular process that must be taken into account in the analysis.

To maintain the lowest possible pressure in the detector chamber, a catcher tube is used inside the chamber, with its orifice $\sim$9 cm from the interaction region. The tube is directly connected to a small pumping chamber and turbopump to efficiently evacuate the gas. This setup makes it possible to keep the detector chamber pressure at $\sim 1\times 10^{-7}$ torr during gas jet operation (compared to 3×10^{-9} torr base pressure). Further improvements in chamber pressure, and reduction in the size of the interaction region, may be possible using a double-skimmer gas jet geometry.

The supersonic nature of the gas jet can be observed directly by the ion detector, and this provides a means to filter the data. Figure 8 shows the x and the y positions of the ion impacts on the delay line detector that will be described later in the text. Two main features are visible in Fig. 8: a line centered on the detector and a small intense region offset in the y direction. The small offset region corresponds to ionization events in the gas jet. The offset comes from the large P_y momentum component of the atoms or molecules from the jet. The centered line, in this case, is simply ionization of the background gas from the EUV beam propagating through the chamber.

Following the work of Miller,[46] the particle density can be estimated for various gases given the nozzle size, skimmer size, distance between nozzle and skimmer, stagnation pressure, etc. For the D_2 experiment presented in Sec. III below, this calculation yields a particle density inside the interaction region of $\sim 10^{11}-10^{12}$ cm^{-3}, which corresponds to an $\sim 10^{-7}-10^{-6}$ torr local pressure. This gas jet local pressure is approximately $1x-10x$ higher than the background pressure in the spectrometer chamber, as shown in Fig. 8.

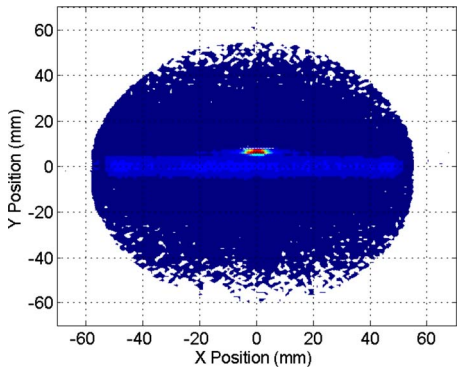

FIG. 8. (Color online) Characterization of the supersonic gas jet through ion velocity displacement. This characterization was done using O_2 gas with 1.5 atm backing pressure, and the ionizing source was 43 eV photons generated by using HHG. The long line across the center of the detection region arises from ionization of the background gas by the EUV beam propagating in the chamber. The more localized and vertically offset intense region arises from the ionization of the gas from the jet, where the molecules have a high initial y momentum component.

F. Guiding electric and magnetic fields

In order to guide the charged particles generated in the interaction region, constant electric and magnetic fields are set up along the axis of the spectrometer. There are three important components (shown in Fig. 6) to the electric field formation: the copper electrodes, the drift region, and the meshes. The copper electrodes surround the detection region. 41 plates are used in conjunction with a resistance chain to establish a uniform field strength (i.e., a constant potential change) in the interaction region. The plates are wired in series by using 100 kΩ resistors, with a typical applied voltage of −200 V on the electron detector side and −400 V on the ion detector side. The negative overall potential, combined with the grounded vacuum chamber, ensures that low energy electrons generated within the chamber but outside the spectrometer region will be excluded from the interaction region, and thus excluded from contributing to the signal. The three central electrodes are cut to allow the laser beam to pass along the x axis, and to allow the gas jet to pass through the y axis. The opening is kept as small as possible to prevent distortion of the electric field. As measured from the center electrode, the acceleration region on the ion detector side is approximately 119 mm long and is approximately 125 mm long on the electron side. The precise lengths depend on laser beam pointing, and must be calibrated by using the detector. The meshes, situated at both ends of the spectrometer and between the copper electrodes and the drift region, are used to ensure that the electric field is constant throughout the spectrometer.

The drift tube consists of a zero electric field region between the copper electrodes and the electron detector. The entire region is typically held at −200 V, corresponding to the voltage of the adjoining copper electrode. The drift tube is approximately twice the length of the electron acceleration region, and its purpose is to temporally focus the electrons. This refocusing makes it possible to reduce systematic error introduced by the extent of the interaction region along the detector axis (z axis) due to the focused laser (EUV or IR) spot size. This method is know as "time-lag focusing."[47]

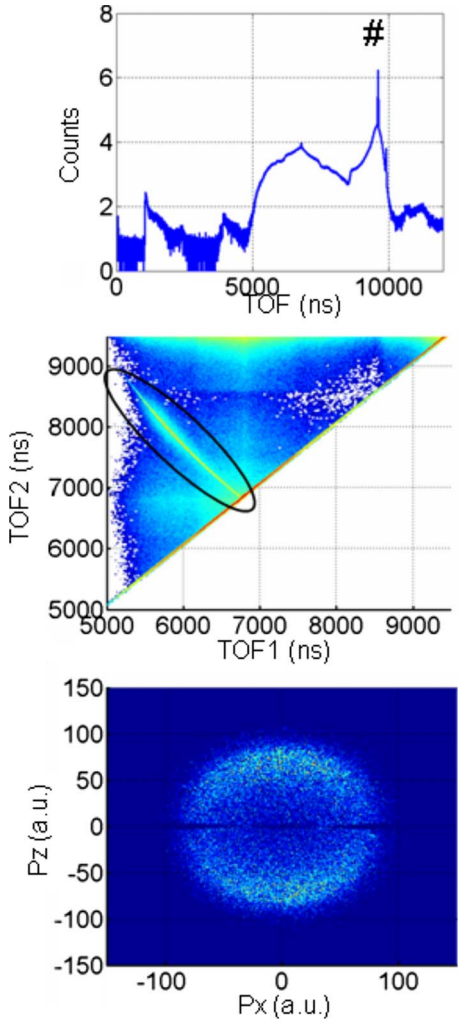

FIG. 9. (Color online) (Top) Time of flight spectrum of O_2 ions when illuminated by both the EUV and IR pulses. # shows the O_2^+ peak. Most of the counts seen in the region between 5000 and 8000 ns correspond to O^+ ions. (Middle) Correlation map between coincident O^+ ions flight times. The off-diagonal feature shows an O_2 dissociation channel. (Bottom) Filtered momentum of the O^+ events that correspond to the dissociation channel of the correlation map. The counts from the dissociation channel are isolated by requiring the O^+ fragments to simultaneously have a nonzero kinetic energy release and a near-zero total momentum.

It is possible to determine the exact values of the electric field (E), the position of the interaction (0,0) in the detector, and the molecular gas jet velocity by looking at the dissociation fragments of the double ionization of a molecule such as O_2 or CO after interaction with an EUV photon. The advantage of using a doubly ionized dissociation process is that the products can be detected relatively background-free. However, most dissociation channels yielding one or more charged fragments are suitable for use in this calibration. In this work, we use the following dissociation:[48]

$$O_2 + h\omega_{\mathrm{EUV}} \rightarrow O_2^{+*} + e \rightarrow O^+ + O^* + e \rightarrow O^+ + O^+ + e + e.$$

This dissociation channel is identified in the time-of-flight (TOF) correlation map between the O^+ fragments (first and second hits) shown in Fig. 9 (middle). These hits can be isolated on the correlation map by employing data filters requiring zero total momentum of the two O^+ ions. Finally, by requiring that the momentum $P_{i.y}$-$P_{i.x}$ cross section [Fig.

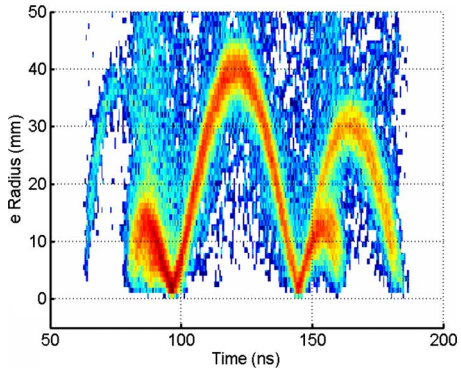

FIG. 10. (Color online) Detected electron radius vs time of flight. The radius is defined as the distance from the center of detector. The nodes are characteristic of the magnetic field and can be used to determine its value

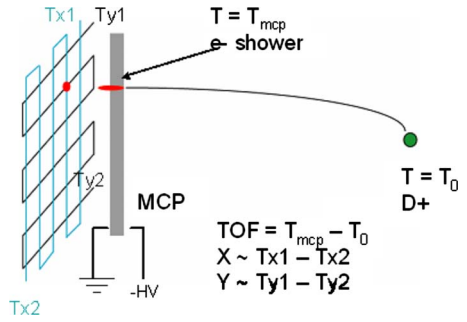

FIG. 11. (Color online) Schematic of the charged fragment detection and momentum calculation. Ionization event occurs at T_0. The charged particle reaches the MCPs at time T_{MCP}. The MCPs generate an electron shower that is collected by a delay line detector behind it. A current pulse is formed and detected at each end of each wire with times Tx1 and Tx2 (for one wire/layer) and with times Ty1 and Ty2 (along the other wire/layer). P_z, P_y, and P_x can then be obtained from TOF, Ty1-Ty2, and Tx1-Tx2, respectively.

9 (bottom)] be circular and centered around (0,0), and using the TOF information [Fig. 9 (top)], one can extract the electric field, the position of interaction, and the gas jet velocity through iterative adjustment.

It should be noted here that the all the information required to calibrate the spectrometer is provided by the apparatus. This self-calibration ability allows us to perform high resolution particle momentum detection, and reduces the probability of systematic errors due to improper calibration. As will be shown later in this section, this self-calibration ability extends to the magnetic field value and absolute time-zero determination as well.

The four coils circling the detector axis were designed to create a constant magnetic field and to confine the energetic electrons. They were constructed of ten gauge square copper wire with 100 turns on each coil. In normal operation, approximately 3 A of current is supplied to these coils. In order to calibrate the magnetic field and time zero, one observes the electron trajectory "nodes" on a plot of electron radius versus TOF, as shown in Fig. 10. By varying the electric field during the data acquisition, multiple nodes can be observed. This plot is often referred to as a "wiggles" plot, referring to the cyclotron orbits of the electron trajectory. If the TOF between two nodes is τ, then the value of the magnetic field B along the z axis is

$$B = \frac{2\pi m_e}{e\tau},$$

where m_e is the electron mass, e is its charge, and τ is the time position of the node. One can then introduce a time offset in the calculation to ensure that the zeroth node be at TOF=0, hence fixing time zero (T_0).

In addition to the magnetic field coils shown in Fig. 6, there are four weaker magnetic field coils in a square pattern around the chamber set to balance the effects of Earth's magnetic field. The current through them is adjusted to ensure that the nodes shown in Fig. 10 are on the axis of the detector (impact radius is zero).

G. Microchannel plates/delay lines

The charged particles impact microchannel plates (MCPs) on each side of the spectrometer that are biased to approximately 2.1–2.3 kV. (Typically, for the ion detector, the front of the MCPs is held at 0 V and the back at 2100 V. For the electron MCPs, the front is held at −50 V and the back at 2200 V.) Each MCP is backed by a wire grid delay line detector (ROENTDEK HANDELS GmbH). The holders for the delay lines have a voltage of 80 and 2280 V for the ion side detector and the electron side detector, respectively. The delay lines themselves consist of alternating signal and reference wires held at 180 and 220 V, respectively, for the ion side and 2380 and 2420 V for the electron side. The electron shower produced by the MCP is collected by the signal wire of the delay line detector where it generates a small current pulse. This current pulse travels to each side of each wire and the time of the signal is recorded and compared to a common fixed trigger signal. This allows us to measure the position of the particle impact. Knowledge of the initial position, TOF, final x and final y positions of the charge particles and of the electric and magnetic fields allows precise determination of the momentum at the time of interaction with the laser pulse (which is shown schematically in Fig. 11).

Each detector consists of a stack of two MCPs in a chevron configuration. Each has an outer diameter of 127 mm and an active diameter of 120 mm (matching the aperture of the copper electrodes).

The electron detector has three layers of delay lines in a hexagonal pattern. The ion detector instead has two layers of delay lines in a square pattern. Only two layers are necessary to determine the position of an electron hit. The third layer, on the electron side, gives redundant information that can be used in the data reconstruction when more than one particle hits the detector during a readout period (approximately 120 ns); i.e., a multihit situation. For both detectors, the electrical signals from the delay lines are sent to RoentDek ATR19 modules, consisting of amplifiers and constant-fraction discriminators. The constant-fraction discriminators are adjusted for each wire to an event-detection threshold. The multihit dead time of the ATR19 module is $\geqslant$20 ns. The ATR generated NIM pulses are sent to eight channel time-to-digital converters (TDCs). The TDCs are based on the LeCroy MTD133B chip. They have a 16 bit dynamic range, a resolution of 500 ps and can be operated to acquire from 1 to 16 hits per trigger event. The multihit dead time for the

TDCs is typically 10 ns. At one hit per channel, a TDC can acquire data at up to 25 kHz. The software package (COBOLD, RoentDek Handels GmbH) reads the data from the TDCs onto the hard disk.

The electronics have a dead time of ~20 ns (mostly determined by the ATRs). If two ions hit the MCP, ten electrical signals will be generated to characterize them fully: two signals from the two ends of the delay line corresponding to the x axis, two signals for the y axis and one signal for the MCP for each ion. In order to detect all ten electrical signals associated with two ions in the same trigger event, they must each be 20 ns apart. Partial detection of the ten electrical signals could be possible if, for example, the two particles hit the MCP within 20 ns (thus at registering the second hit in the MCP channel) but at sufficiently different positions so that they can be detected by the delay line anode. Alternatively, the MCP signals might be more than 20 ns apart but the position of each hit is such that one or more of the delay line channels would miss the second hit. Since a "full" event contains redundant information, partially detected hits can be reconstructed to fill in the missing information using a software algorithm (COBOLD). For ions, given the typically long TOF involved, the multihit dead time is usually not a significant restriction for two-particle detection. However, it can become important for electron detection. That is the reason a three layer delay line is used for electrons. The third layer provides another set of redundant electrical signals that can be used for data reconstruction by the software.

H. Experimental considerations

A detailed analysis of the uncertainty in COLTRIMS apparatus was covered by Dörner *et al.*[24] in a previous publication. In this article, we will discuss a source of energy uncertainty in the detected charged particles specific to our setup: the extended interaction region. As we described above, the interaction region inside the spectrometer is approximately 150 μm in diameter, perpendicular to the laser axis, and 4 mm long along the laser axis. This extended interaction region, which results in an uncertainty in the initial position of the molecular reaction, will result in an uncertainty in the energy of the detected particles. The exact uncertainty in energy is of course different for ions and electrons. It is dependent on a number of factors: the value of the electric field, the value of the magnetic field (for electrons), and the angular distribution of the charged particles.

For example, oxygen ions in a 916 V/m electric field, with 3 eV kinetic energy, and with a cosine-square distribution along the P_y axis have a ± 0.13 eV detected energy uncertainty. If the cosine square is along the P_z axis, the uncertainty is ± 0.1 eV. For electrons, the situation is further complicated by the presence of the magnetic field. For a 25 eV electron, with similar electric field as the oxygen ions, a magnetic field value of 6.37 G, and similar angular distribution, the energy uncertainty is on the order of ± 0.8 eV for a cosine-square distribution along the P_y axis and approximately ± 0.3 eV for a cosine-square distribution along the P_z axis. This number fortunately becomes much smaller when looking at low energy electrons. For 1.5 eV electrons, with an electric field of 238 V/m, and a magnetic field of 3.37 G,

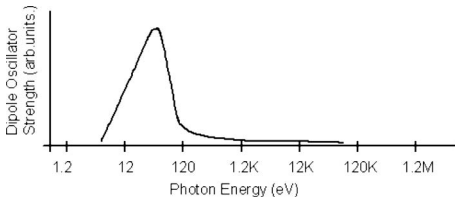

FIG. 12. Dipole oscillator strength calculated for varying photon energy (Ref. 49).

the energy uncertainty for a cosine-square distribution along the P_y axis is ± 0.1 eV. For a cosine-square distribution along the P_z axis, the uncertainty in the electrons becomes ± 0.07 eV. The previous values were all obtained by varying the input parameters of the equations of motion of the charged particles inside the spectrometer.

It should be noted that the uncertainty values are smaller in all cases when the charged particles are ejected along the laser polarization axis (z axis). However, the computer simulation used to calculate the uncertainty values presented so far also indicates that the value of the magnetic field is critical when dealing with electrons. For an improperly set magnetic field, the uncertainty in the electron energy, for a cosine-square distribution along the P_z axis, can become much greater than that along the P_y axis. These uncertainty values could be greatly improved by the implementation of a double-skimmer geometry that could reduce the size of the interaction region within the spectrometer.

Another important experimental consideration is the count rate. The coincidence capability of the detector is critical for allowing complete reconstruction of the momentum of all the particles involved in a laser-initiated reaction. However, the coincidence requirement does place a limit on the count rate in order to match a detected ion with a detected electron. If more than one ionization event occurs per laser shot, it becomes increasingly difficult to determine which ions came in coincidence with which electrons.

The three factors that determine the count rate are the flux in the EUV pulse, the gas density, and the molecular absorption cross section. The multilayer mirrors select the 27th harmonic of the 800 nm fundamental laser light, corresponding to an ~43 eV photon energy. After two reflections from the multilayer mirrors and transmission through a 200 nm thick aluminum filter, about $\sim 10^6$ photons/pulse are focused to the interaction region. Given the typical absorption cross section for molecules in the 10–100 eV region of the spectrum of ~1–100 Mbytes, and the typical gas density of 10^{11} cm^{-3}, this results in a count rate on the order of one event per pulse. A typical atomic and molecular cross sections peak in the 10 eV–keV range of photon energies[49] is shown in Fig. 12.

The most severe limitation in most experiments using this apparatus is the event count rate, which is limited by the pulse repetition rate. In most experiments, the channel to be observed will represent only a small fraction of the total ionization events. It is not rare that, even for an overall event count rate nearing the 2 kHz repetition rate of the laser, the count rate for a specific channel will be of the order of 10–1000 events/h. For pump/probe measurements, where a

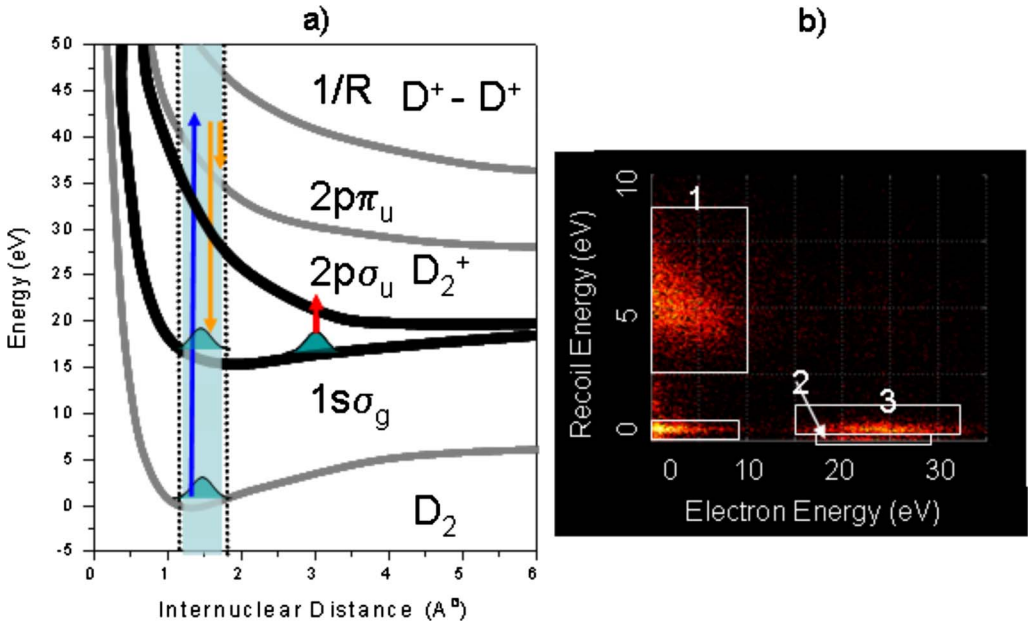

FIG. 13. (Color online) Correlation data for two-color EUV/IR excitation and ionization of the D_2 molecule. (a) The potential energy diagram for D_2 molecule showing ground state, D_2^+ ground and excited states and D_2^{2+} state. The EUV pulse is represented by the long upward blue arrow. The detected electron energy associated with populating a particular state is shown by the downward orange arrows. The IR ionization is represented by the short upward red arrow. (b) The ion-energy/electron-energy correlation map obtained by using the reaction microscope, showing different channels.

complete data set is necessary for a sequence of pump-probe time delays, the experiment might demand up to 100 h (or even more) of continuous data acquisition. While the laser system is stable enough for such run, an increase in the data rate would be desirable. This can only be achieved by increasing the laser repetition rate. Increasing the pulse energy might also increase the count rate, but the number of counts per laser shot would become more than one and the coincidence capability would be lost. A 20 kHz repetition-rate laser system, for example, with a similar per pulse energy as the 2 kHz system would reduce the acquisition time by a factor of 10 and would also make possible experiments where the molecular cross section is low. The TDCs can be operated at up to 25 kHz. This would make a 20 kHz system near ideal for this COLTRIMS setup.

III. RESULTS D_2

As an example of the capabilities of this tabletop EUV reaction microscope, we consider the excitation and dissociation of a D_2 molecule. This experiment makes use of two-color excitation—an EUV pulse is used to photoionize D_2 to the D_2^+ ion in the ground and excited states, with an intense 800 nm infrared pulse overlapped both spatially and temporally (no time delay) with the EUV pulse. The photoionization cross section for D_2, in particular, is quite low at 43 eV (<1 Mbytes) making this a particularly challenging system to study. However, since D_2 is a relatively simple molecule, the data are easier to interpret, making D_2 an attractive candidate for initial studies. The bound and repulsive states of D_2^+ formed after photoionization evolve with time, and this evolution is represented in terms of potential energy curves. Since the D_2^+ is a simple molecule, calculations can determine reliable potential energy curves, as shown in Fig. 13(a).[50] Based on this potential energy diagram, we can employ our coincidence momentum imaging techniques to isolate and identify different excitation and dissociation channels.

Figure 13(b) shows three main groupings in the electron energy-ion energy correlation map. Here, the x axis corresponds to the kinetic energy of the detected electron, while the y axis corresponds to the kinetic energy of the coincident detected ion. Group 1 corresponds to photoelectrons with energies around 3 eV. Since we use EUV photon energies around 43 eV, this implies that we are exciting electronic states around $43-3=40$ eV. This corresponds to excitation of the $2p\pi_u$ state of D_2^+. This excited state is strongly dissociative and asymptotically approaches a limit at ~ 31 eV in potential energy. This limit corresponds to two fragments, D and D^+, with a total energy of $40-31=9$ eV. Since the two fragments share energy equally in the kinetic energy release, we should observe ion energies of around 4.5 eV for this process. This is exactly what we observe in group 1 shown in the correlation map of Fig. 13(b). Hence, this feature corresponds to dissociation dynamics of the $2p\pi_u$ electron state created by soft-x-ray photoionization. The momentum distribution, P_x versus P_y, for this dissociation process is also shown [Fig. 14 (top)]. We observe the ion fragments flying out normal to the soft-x-ray polarization. This also confirms our interpretation since $2p\pi_u$ formation corresponds to a perpendicular transition in which molecules perpendicular to photon polarization are preferentially ionized.

The second feature in Fig. 13(b) represents a small amount of dissociation arising from a D_2^+ wave packet evolving in the potential well of the $1s\sigma_g$ state. Again, energy conservation arguments can be used to confirm that we should observe electron of energy $43-16=27$ eV, and very low energy ions. The momentum distribution for this channel is uniform, as shown in Fig. 14 (middle).

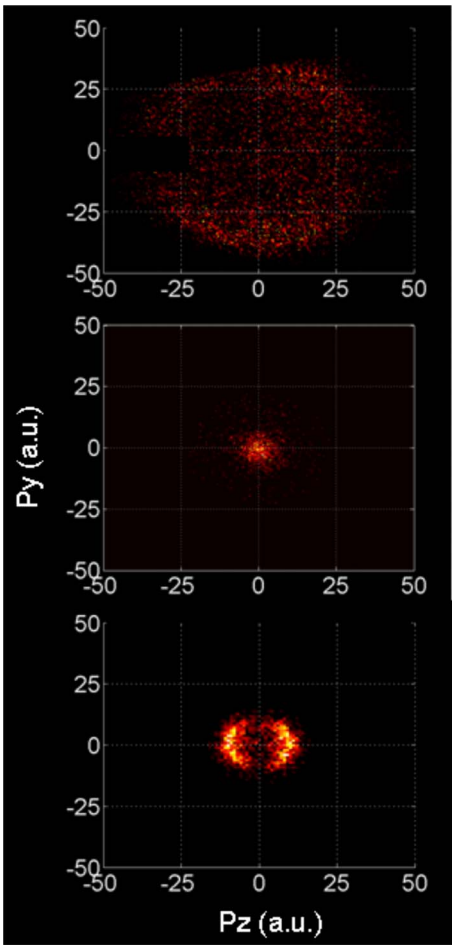

FIG. 14. (Color online) Momentum distributions for different dissociative channels. The x axis shows the momentum component along the axis of the detector (labeled z axis) and the y axis, the y component of the momentum. The laser polarization is along the axis of the detector (z axis). (Top) $2p\pi_u$. (Middle) $1s\sigma_g$. (Bottom) EUV ionization to the $1s\sigma_g$ potential energy curve followed by IR excitation to the $2p\sigma_u$ potential energy curve.

Next, we address the third feature observed in Fig. 13(b). It is populated when we use an IR pulse as a probe field. As described earlier, we use EUV light to form D^+ in the $1s\sigma_g$ state. This photoionization is accompanied by the launch of a vibrational wave packet in the associated potential well. This vibrational wave packet evolves with periodicity of 22 fs. Due to its coherent nature, it slowly dephases and rephases as function of time.[51] This bound vibrational wave packet can be interrupted by using an IR pulse to cause bond softening. The IR pulse modifies the potential energy curves and leads to dissociation of excited vibrational states. This transition from $1s\sigma_g$ to $2p\sigma_u$ is schematically represented in Fig. 13(a) by a red photon, which initiates a one photon process at certain internuclear distances. The dissociation from the $2p\sigma_u$ state at this internuclear distance leads to low recoil energy ($\sim$0.4 eV) D^+ ions, which we observe in our correlation map. The signature of bond softening is ion emission highly peaked along the laser polarization, as shown in Fig. 14 (bottom).

Finally, the feature near the origin (0,0) of the energy correlation map is also due to bond softening. However, it results entirely from the strong-field IR pulse—i.e., multiphoton dissociation—and the EUV beam plays no role.

By using our COLTRIMS detector, we have thus observed all of the major excitation and dissociation channels for the case of photoionization of D_2 by a 43 eV EUV pulse.[50,51] The novelty of this technique becomes apparent when it is used to access femtosecond dynamics of inner-valence electrons and highly excited state of molecules, which is not possible using other spectroscopic techniques.

In a separate experiment,[21] we performed such a study of the dissociation dynamics of shake-up state in N_2. An EUV beam, with a 43 eV photon energy, was used to populate a highly excited, dissociative N_2^+ state. An IR pulse was then used to probe the nuclear dynamics as the molecule exploded. The results were matched by a theoretical calculation indicating that a shake-up state of N_2 was being probed. This allows us to observe a molecular system as it evolves with femtosecond temporal and atomic-scale spatial resolution. Similar experiments are also being performed in various other molecules.

IV. CONCLUSION AND FUTURE WORK

In conclusion, we have presented a novel experimental setup that makes it possible for the first time to explore highly excited molecular dynamics on femtosecond to attosecond time scales. The essential constituents of this system are femtosecond EUV pulses obtained from high harmonics, and the coincident three-dimensional momentum imaging method that serves as a reaction microscope. This system has allowed us to perform the first femtosecond studies of molecular dynamics initiated by ionizing radiation. The implementation of the techniques discussed here will make possible many new experiments in the area of radiation femtochemistry.

Future experiments will include exploring different molecular systems, specifically O_2 and CO, where the 43 eV photon energy is near the double ionization potential. This makes these systems ideal to probe by using combined EUV and IR radiation. Changing the EUV photon energy, by changing the multilayer mirrors, will also make it possible to probe different molecular states. Finally, improvements in the laser source (higher repetition rate and carrier-envelope stabilization) will give us access to molecules and molecular states with smaller cross sections, and open the way to carrier envelope phase sensitive experiments.

ACKNOWLEDGMENTS

We acknowledge support for this work from the NSF through the Physics Frontiers Centers Program and from the Department of Energy, Office of Science. This work made use of facilities provided by the NSF Engineering Research Center on Extreme Ultraviolet Science and Technology.

APPENDIX: GENERATION OF SUB-OPTICAL CYCLE EUV PULSES

In this appendix, we discuss the generation of an efficient, tunable, and suboptical cycle EUV source that further improves the time resolution capabilities and bandwidth se-

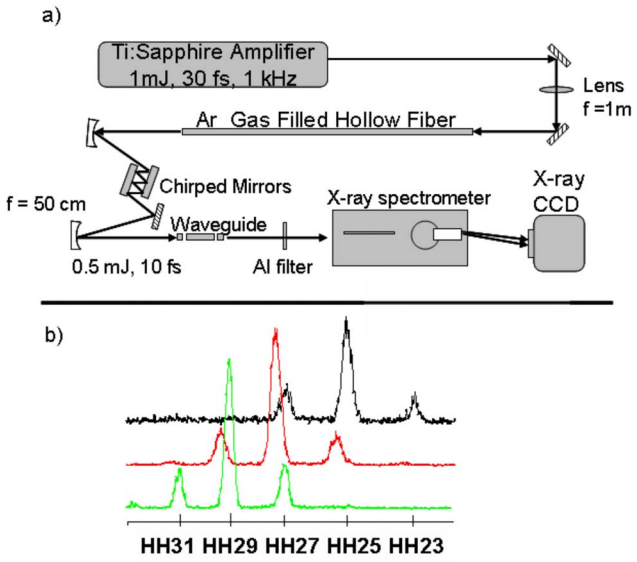

FIG. 15. (Color online) (a) Experimental schematic for the EUV pulse characterization. The amplifier laser beam is focused into a 1 m long argon-filled hollow core fiber. The spectrum of the pulse is broadened through SPM. The waveguide output is compressed in time by using a pair of chirped mirrors. The resulting 10–12 fs pulse is focused into another hollow waveguide to create and EUV beam through HHG. The output beam is analyzed by using an x-ray spectrometer and CCD camera. (b) Narrow pressure dependent x-ray spectrum. The green curve corresponds to 78 torr of argon in the HHG waveguide with an intensity of 2.0×10^{14} W/cm^2. The harmonic emission is centered at the 29th harmonic. The red curve corresponds to 50 torr of argon in the HHG waveguide with an intensity of 1.8×10^{14} W/cm^2. The harmonic emission is centered at the 27th harmonic. The black curve corresponds to 32 torr of argon in the HHG waveguide with an intensity of 1.7×10^{14} W/cm^2. The harmonic emission is centered at the 25th harmonic.

lectivity of these sources without sacrificing the flux. It is based on the phase matched conversion of 800 nm into the EUV in a hollow waveguide filled with Ar gas.[38,40,52]

Short pulse generation

We generate the EUV beam in two different regimes. In the first case, which was discussed above, we send the 30 fs, 2 mJ pulses from the ultrafast laser system directly into the 2.5 cm EUV waveguide. In the second case, discussed here, we first spectrally broaden the pulse using self-phase modulation (SPM) and then compress it by using chirped mirror recompression,[53] before sending it to the EUV waveguide. SPM is achieved by propagating the laser pulse through a 400 μm inner-diameter waveguide filled with Ar or Ne (see Fig. 15). The waveguide is held straight in a V-groove mount with vacuum seals on each end. The design is similar to the EUV waveguide holder that was discussed earlier in the text. In the case of Ar, a gas pressure gradient is applied to the waveguide with the pressure at the entrance at ~1 torr, and at the exit between 100 and 350 torr. This gradient is used to enhance the laser coupling into the waveguide by avoiding defocusing due to plasma generation before the entrance.[54] When neon was used, the pressure was kept constant throughout the waveguide at 100–300 torr. Its higher ionization potential (21.6 eV for Ne compared to 15.7 eV for Ar) reduces the plasma generation before the entrance of the

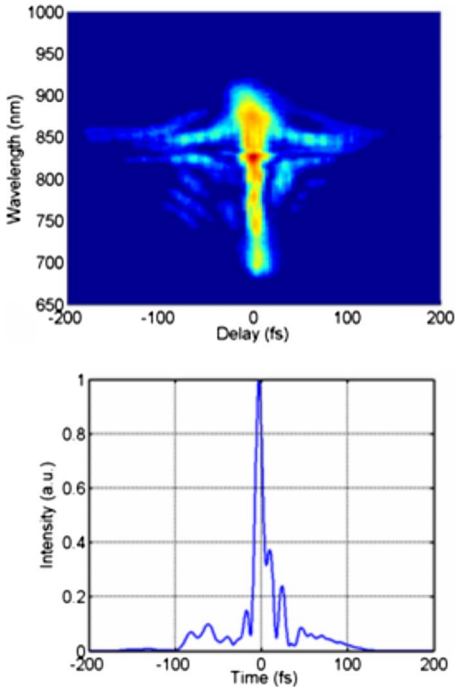

FIG. 16. (Color online) (Top) Sample GRENOUILLE trace of the pulse after spectral broadening in the SPM waveguide and recompression with the chirped mirrors. (bottom) Reconstruction of the temporal profile of the pulse from the GRENOUILLE trace by using a standard FROG algorithm showing a 10–12 fs pulse.

waveguide without the need for low gas pressure. We found that for self-phase modulation of pulses with energies higher than 1 mJ, Ne is the better solution.

After exiting the SPM waveguide, the beam is sent to a pair of chirped mirrors. These are Layertec GmbH mirrors with 60 fs^2 of group velocity dispersion per bounce. Six bounces are enough to recompress the pulse. Fine adjustments to the pulse duration were performed by changing the gas pressure. Figure 16 shows the reconstructed pulse obtained after the SPM waveguide. The trace was acquired with a 10 fs GRENOUILLE from Swamp Optics, that uses a frequency-doubling crystal that is swiveled to cover a broad spectral range of second harmonic generation while also using a relatively thick doubling crystal. The trace obtained can be converted to deconvolve by using a standard FROG algorithm.

After compression, the total efficiency is approximately 40%. This efficiency is primarily determined by the SPM waveguide throughput in its lowest-order mode. Additional loss also occurs due to the reflective efficiency of the chirped mirrors. This system results in a pulse energy of 0.75–0.85 mJ with a 10–12 fs pulse duration.

EUV results

Using the output from this system, the EUV emission spectrum was characterized previously[55] by using an x-ray spectrometer and charge coupled device (CCD) camera, as shown in Fig. 15(a). We find that we can generate a very tunable source of narrow-band harmonic emission consisting primarily of one harmonic order. In addition, this emission is temporally confined to ~1 fs, further improving the time res-

olution capabilities of our experiment.[56] The mechanism of this time-and-spectrally selective phase matching is discussed below.

Intense 10 fs duration laser pulses propagating in a hollow waveguide can experience a nonlinear stabilization mechanism arising from the interplay between the transient plasma generated by the laser and the instantaneous laser intensity. This stabilization results in a narrow phase matching window for high harmonic emission, which has unique advantages, both in temporal and spectral domains. For gas pressures between 30 and 80 torr, and for laser intensities around $\sim(1.7-2.0)\times 10^{14}$ W cm^{-2}, the EUV radiation can be primarily localized to a single harmonic accompanied by two relatively weak neighboring harmonics. In the spectral domain, as Fig. 15(b) shows, by simple tuning of the pressure and the laser intensity, various single harmonic orders (e.g., 25th, 27th, and 29th) can be selectively optimized. This behavior is in contrast to longer >20 fs pulses where a comb of ≈ 7 harmonic orders is generated, and where all harmonics optimize under nearly the same pressure and intensity conditions. This method thus provides us with a selective and tunable photon source which has many applications in atomic and molecular spectroscopies. In this case, energy selectivity is obtained without the use of relatively inefficient, wavelength selective, optics/gratings. Further, by using this technique, one can confine the high harmonic emission to a very narrow suboptical cycle temporal window. The full energy spectrum exiting the waveguide, i.e., a single main harmonic along with two satellites, corresponds to a short attosecond burst with weak satellites, and the entire emission is confined to less than 2 fs irrespective of the carrier-envelope phase of the driving laser.[56] Thus, for applications requiring high time resolution, one can directly utilize the EUV emission from the waveguide in pump-probe experiments without the need for spectral filtering of the EUV emission or the phase stabilization of the amplifier system. These observations represent a new way to generate tunable, femtosecond, isolated EUV pulses that will have many applications as a probe of ultrafast molecular and electronic dynamics.

[1] A. L'Huillier and P. Balcou, Phys. Rev. Lett. **70**, 774 (1993).
[2] Ch. Spielmann, N. H. Burnett, S. Sartania, R. Koppitsch, M. Schnurer, C. Kan, M. Lenzner, P. Wobrauschek, and F. Krausz, Science **278**, 661 (1997).
[3] Z. Chang, A. R. Rundquist, H. Wang, M. M. Murnane, and H. C. Kapteyn, Phys. Rev. Lett. **79**, 2967 (1997).
[4] I. P. Christov, M. M. Murnane, and H. C. Kapteyn, Phys. Rev. Lett. **78**, 1251 (1997).
[5] A. Scrinzi, M. Yu Ivanov, R. Kienberger, and D. M. Villeneuve, J. Phys. B **39**, R1 (2006).
[6] H. C. Kapteyn, M. M. Murnane, and I. P. Christov, Phys. Today **58**, 39 (2005).
[7] G. Sansone, E. Benedetti, F. Calegari, C. Vozzi, L. Avaldi, R. Flammini, L. Poletto, P. Villoreso, C. Altucci, R. Velotta, S. Stagira, S. De Silvestri, and N. Nisoli, Science **314**, 443 (2006).
[8] A. Zair, A. Guandalini, F. Schapper, M. Holler, J. Biegert, L. Gallmann, A. Couairon, M. Franco, A. Mysyrowicz, and U. Keller, Opt. Express **15**, 5394 (2007).
[9] A. Baltuska, T. Udem, M. Uiberacker, E. Goulielmakis, C. Gohle, R. Holzwarth, V. S. Yakovlev, A. Scrinzi, T. W. Hansch, and F. Krausz, Nature (London) **421**, 611 (2003).
[10] E. Gagnon, I. Thomann, A. Paul, A. L. Lytle, S. Backus, M. M. Murnane, H. C. Kapteyn, and A. S. Sandhu, Opt. Lett. **31**, 1866 (2006).
[11] T. Imran, Y. Soo Lee, C. H. Nam, K.-H. Hong, T. J. Yu, and J. H. Sung, Opt. Express **15**, 104 (2007).
[12] A. H. Zewail, Science **242**, 1645 (1988).
[13] O. Gessner, A. M. D. Lee, J. P. Schaffer, H. Reisler, S. V. Levchenko, A. I. Krylov, J. G. Underwood, H. Shi, A. L. L. East, D. M. Wardlaw, E. t. H. Chrysostom, and A. Stolow, Science **311**, 219 (2006).
[14] A. M. Rijs, M. H. M. Janssen, E. t. H. Chrysostom, and C. C. Hayden, Phys. Rev. Lett. **92**, 123002 (2004).
[15] M. H. Kim, L. Shen, H. Tao, T. J. Martinez, and A. G. Suits, Science **315**, 1561 (2007).
[16] A. Stolow, A. E. Bragg, and D. M. Neumark, Chem. Rev. (Washington, D.C.) **104**, 1719 (2004).
[17] S. Zamith, V. Blanchet, B. Girard, J. Andersson, S. L. Sorensen, I. Hjelte, O. Björneholm, D. Gauyacq, J. Norin, J. Mauritsson, and A. L'Huillier, J. Chem. Phys. **119**, 3763 (2003).
[18] S. Voss, A. S. Alnaser, X. M. Tong, C. Maharjan, P. Ranitovic, B. Ulrich, B. Shan, Z. Chang, C. D. Lin, and C. L. Cocke, J. Phys. B **37**, 4239 (2004).
[19] R. R. Meier, Space Sci. Rev. **58**, 1 (1991).
[20] H. Imanaka and M. A. Smith, Geophys. Res. Lett. **34**, L02204 (2007).
[21] E. Gagnon, P. Ranitovic, X. M. Tong, C. L. Cocke, M. M. Murnane, H. C. Kapteyn, and A. S. Sandhu, Science **317**, 1374 (2007).
[22] V. Ayvazyan, N. Baboi, J. Bahr, V. Balandin, B. Beutner, A. Brandt, I. Bohnet, A. Bolzmann, R. Brinkmann, O. I. Brovko, J. P. Carneiro, S. Casalbuoni, M. Castellano, P. Castro, L. Catani, E. Chiadroni, S. Choroba, A. Cianchi, H. Delsim-Hashemi, G. Di Pirro, M. Dohlus, S. Dusterer, H. T. Edwards, B. Faatz, A. A. Fateev, J. Feldhaus, K. Flottman, J. Frisch, L. Frohlich, T. Garvey, U. Gensch, N. Golubeva, H. J. Grabosch, B. Grigoryan, O. Grimm, U. Hahn, J. H. Han, M. V. Hartrott, K. Honkavaara, M. Huning, R. Ischebeck, E. Jaeschke, M. Jablonka, R. Kammering, V. Katalev, B. Keitel, S. Khodyachykh, Y. Kim, V. Kocharyan, M. Korfer, M. Kollewe, D. Kostin, D. Kramer, M. Krassilnikov, G. Kube, L. Lilje, T. Limberg, D. Lipka, F. Lohl, M. Luong, C. Magne, J. Menzel, P. Michelato, V. Miltchev, M. Minty, W. D. Moller, L. Monaco, W. Muller, M. Nagl, O. Napoly, P. Nicolosi, D. Nolle, T. Nunez, A. Oppelt, C. Pagani, R. Paparella, B. Petersen, B. Petrosyan, J. Pfluger, P. Piot, E. Plonjes, L. Poletto, D. Proch, D. Pugachov, K. Rehlich, D. Richter, S. Riemann, M. Ross, J. Rossbach, M. Sachwitz, E. L. Saldin, W. Sandner, H. Schlarb, B. Schmidt, M. Schmitz, P. Schmuser, J. R. Schneider, E. A. Schneidmiller, H. J. Schreiber, S. Schreiber, A. V. Shabunov, D. Sertore, S. Setzer, S. Simrock, E. Sombrowski, L. Staykov, B. Steffen, F. Stephan, F. Stulle, K. P. Sytchev, H. Thom, K. Tiedtke, M. Tischer, R. Treusch, D. Trines, I. Tsakov, A. Vardanyan, R. Wanzenberg, T. Weiland, H. Weise, M. Wendt, I. Will, A. Winter, K. Wittenburg, M. V. Yurkov, I. Zagorodnov, P. Zambolin, and K. Zapfe, Eur. Phys. J. D **37**, 297 (2006).
[23] J. Chalupsky, L. Juna, J. Kuba, J. Cihelka, V. Hajkova, S. Koptyaev, J. Krasa, A. Velyhan, M. Bergh, C. Caleman, J. Hajdu, R. M. Bionta, H. Chapman, S. P. Hau-Riege, R. A. London, M. Jurek, J. Krzywinski, R. Nietubyc, J. B. Pelka, R. Sobierajski, J. Meyer-ter-Vehn, A. Tronnier, K. Sokolowski-Tinten, N. Stojanovic, K. Tiedtke, S. Toleikis, T. Tschentscher, H. Wabnitz, and U. Zastrau, Opt. Express **15**, 6036 (2007).
[24] R. Dörner, V. Mergel, O. Jagutzki, L. Spielberger, J. Ullrich, R. Moshammer, and H. Schmidt-Böcking, Phys. Rep. **330**, 96 (2000).
[25] H. Schmidt-Böcking, M. S. Schöffer, T. Jahnke, A. Czasch, V. Mergel, L. Schmidt, R. Dörner, O. Jagutzki, M. Hattass, Th. Weber, E. Weigold, H. T. Schmidt, R. Schuch, H. Cederquist, Y. Demkov, C. Whelan, A. Gudonov, and J. Walters, Nucl. Instrum. Methods Phys. Res. B **233**, 3 (2005).
[26] R. Moshammer, M. Unverzagt, W. Schmitt, J. Ullrich, and H. Schmidt-Böcking, Nucl. Instrum. Methods Phys. Res. B **108**, 425 (1996).
[27] E. A. Gibson, A. Paul, N. Wagner, R. Tobey, S. Backus, I. P. Christov, M. M. Murnane, and H. C. Kapteyn, Phys. Rev. Lett. **92**, 033001 (2004).
[28] A. McPherson, G. Gibson, H. Jara, U. Johann, T. S. Luk, I. A. McIntyre, K. Boyer, and C. K. Rhodes, J. Opt. Soc. Am. B **4**, 595 (1987).
[29] A. L'Huillier, Ph. Balcou, and L. A. Lompré, Phys. Rev. Lett. **68**, 166 (1992).
[30] J. Zhou, J. Peatross, M. M. Murnane, and H. C. Kapteyn, Phys. Rev. Lett. **76**, 752 (1996).
[31] E. Seres, J. Seres, F. Krausz, and C. Spielmann, Phys. Rev. Lett. **92**, 163002 (2004).
[32] D. E. Spence, P. N. Kean, and W. Sibbett, Opt. Lett. **16**, 42 (1991).
[33] M. T. Asaki, C. P. Huang, D. Garvey, J. P. Zhou, H. C. Kapteyn, and M. M. Murnane, Opt. Lett. **18**, 977 (1993).
[34] S. Backus, J. Peatross, C. P. Huang, M. M. Murnane, and H. C. Kapteyn, Opt. Lett. **20**, 2000 (1995).

[35] S. Backus, C. G. Durfee, III, M. M. Murnane, and H. C. Kapteyn, Rev. Sci. Instrum. **69**, 1207 (1998).
[36] K. C. Kulander, *Proceedings on SILAP III*, edited by B. Piraux (Plenum, New York, 1993).
[37] P. B. Corkum, Phys. Rev. Lett. **71**, 1994 (1993).
[38] A. Rundquist, C. G. Durfee, III, Z. Chang, C. Herne, S. Backus, M. M. Murnane, and H. C. Kapteyn, Science **280**, 5368 (1998).
[39] A. Paul, E. A. Gibson, X. Zhang, A. Lytle, T. Popmintchev, X. Zhou, M. M. Murnane, I. P. Christov, and H. C. Kapteyn, IEEE J. Quantum Electron. **42**, 14 (2006).
[40] C. G. Durfee, III, A. R. Rundquist, S. Backus, C. Herne, M. M. Murnane, and H. C. Kapteyn, Phys. Rev. Lett. **83**, 2187 (1999).
[41] E. A. J. Marcatili and R. A. Schmeltzer, Bell Syst. Tech. J. **43**, 1783 (1964).
[42] A. Paul, Ph.D. thesis, University of Colorado at Boulder, 2007.
[43] L. Poletto and P. Villoresi, Appl. Opt. **45**, 8577 (2006).
[44] A. L'Huillier, K. Schafer, and K. C. Kulander, J. Phys. B **24**, 3315 (1991).
[45] J. Wildenauer, J. Appl. Phys. **62**, 41 (1987).
[46] D. Miller, in *Atomic and Molecular Beam Methods*, edited by G. Scoles (Oxford University Press, New York, 1988), Vol. 1, pp. 14–53.
[47] W. C. Wiley and I. H. McLaren, Rev. Sci. Instrum. **26**, 1150 (1955).
[48] R. Feifel, J. H. D. Eland, and D. Edvardsson, J. Chem. Phys. **122**, 144308 (2005).
[49] Y. Hatano, J. Electron Spectrosc. Relat. Phenom. **119**, 107 (2001).
[50] T. Aoto, Y. Hikosaka, R. I. Hall, K. Ito, J. Fernandez, and F. Martin, Chem. Phys. Lett. **389**, 145 (2004).
[51] A. Rudenko, Th. Ergler, B. Feuerstein, K. Zrost, C. D. Schröter, R. Moshammer, and J. Ullrich, Chem. Phys. **329**, 193 (2006).
[52] A. Paul, R. A. Bartels, R. Tobey, H. Green, S. Weiman, I. P. Christov, M. M. Murnane, H. C. Kapteyn, and S. Backus, Nature (London) **421**, 6918 (2003).
[53] N. Nisoli, S. De Silvestri, O. Svelto, R. Szipocs, K. Ferencz, Ch. Spielmann, S. Sartania, and F. Krausz, Opt. Lett. **22**, 522 (1997).
[54] N. Nurhuda, A. Suda, M. Kaku, and K. Midorikawa, Appl. Phys. B: Lasers Opt. **89**, 209 (2007).
[55] A. S. Sandhu, E. Gagnon, A. Paul, I. Thomann, A. Lytle, T. Keep, M. M. Murnane, and H. C. Kapteyn, Phys. Rev. A **74**, 061803 (2006).
[56] I. Thomann, E. Gregonis, M. Murnane, and H. Kapteyn, "Temporal Characterization of Energy-Tunable EUV Pulses in the Sub-Optical-Cycle Regime Using FROG-CRAB", in *Conf. on Lasers and Electro-optics (CLEO/QELS)*, Baltimore, MD, 2007, Paper CPDB4.